



Numerical modeling and validation for 3D coupled-nonlinear thermo-hydro-mechanical problems in masonry dams



Long Nguyen-Tuan^{a,*}, Carsten Könke^a, Volker Bettzieche^b, Tom Lahmer^a

^a Institute of Structural Mechanics, Bauhaus-Universität Weimar, Germany

^b Department of Dam Maintenance and Geotechnics, Ruhrverband, Germany

ARTICLE INFO

Article history:

Received 7 April 2016

Accepted 4 October 2016

Keywords:

Coupled thermo-hydro-mechanical analysis

Masonry dam

Unsaturated condition

Water infiltration

Parallel computation

Conjugate Gradient Squared method

ABSTRACT

We introduce in this article a fully coupled thermo-hydro-mechanical (THM) model describing the physical phenomenon present in masonry materials. A series of 3D numerical simulations are carried out for the THM analysis of a dam during its impounding process. The results of the coupled THM analyzes are validated with measurements recorded during that process in terms of transient displacement, pore-water pressure and temperature values. An agreement between numerical simulations and measured data proves that the coupled THM model can well reproduce the multi-physical behavior of masonry dams. Furthermore, we introduce herein a solution for a large system of balance equations by combining parallel computation, storage in Compressed Sparse Row format, and iterative pre-conditioned Conjugate Gradient Squared method in order to improve the computational cost.

© 2016 Elsevier Ltd. All rights reserved.

1. Introduction

Many masonry dams were built at the beginning of the twentieth century e.g. Fürwigge Dam and Ennepe Dam in Germany, and the Theodore Roosevelt Dam in Arizona, USA. After more than one hundred years, the waterproof layers at the upstream side of the dam and the vertical drainage system may be damaged. Additionally, material properties of the dam body were also changed due to ageing, weathering and chemical effects. Consequently, there is a significant amount of water seeping from the upstream side to the downstream side of the dam.

In order to extend the dam operation, rehabilitation processes are carried out. Some common methods are to construct a drainage net of boreholes in the dam body and to repair the waterproof layers. Besides that, measurement devices and sensors are installed in order to monitor the physical behavior of the dam (i.e. deformation, pore-water pressure, effective stress, temperature) [1,2]. Generally, masonry dams have to bear three major loads. The first and most obvious type of load is water pressure and the second load is self-weight load. Thirdly, the temperature load on the dam structure varies according to the water and air temperatures. This causes the stresses within the structure and deformation of the dam. According to the measurement reports [1,3], the effects of

temperature on the deformation of the dam and water infiltration are significant.

Therefore, the mutual relations among thermal conduction, water transport in unsaturated media and force-deformation have to be considered simultaneously while performing numerical simulations of the dams. Moreover, the geometry of dams often has an arch form, with complex geometrical boundaries, which minimizes the bending moments in the dam body. In order to analyze precisely the behaviors and processes occurring in the dam body, the numerical simulation as a fully coupled thermo-hydro-mechanical (THM) analysis in three-dimensional models is necessary.

Coupled numerical simulations of water transport with stress-strain relations in saturated porous media applied to dams were introduced in Wang et al. [4] and considering the cracks or damages in the media, e.g. in [5,6] and multi-phase flows in unsaturated porous media, e.g. in [7–9]. However, modeling the water infiltration and deformation for the dams considering the intertwined effects of temperature is still missing. We note that several multi-physical models of coupled THM problems for soils and porous media have been introduced, e.g. in [10–12].

A 3D coupled THM problem requires five degrees of freedom per node (three for displacements, one for pore water pressure and one for temperature). The dam with complex geometry requires a large set of elements. Consequently, if the problem is solved with LU factorization using band storage format, the computational cost will be extremely high. Therefore, we introduce a

* Corresponding author.

E-mail address: long.nguyen.tuan@uni-weimar.de (L. Nguyen-Tuan).

URL: <http://www.uni-weimar.de/ism>.

Nomenclature

Ω	domain analysis, first used in Eq. (19)	D_m	diffusion coefficient of vapor, first used in Eq. (15)
α_T	coefficient of thermal expansion, first used in Eq. (10)	\mathbf{D}^e	elastic material matrix of the solid phase, first used in Eq. (8)
α_s	coefficient of swelling/shrinkage induced by suction, first used in Eq. (10)	E	elastic modulus, first used in Eq. (8)
λ_T	thermal conductivity, first used in Eq. (2)	e	void ratio, first used in Eq. (1)
λ_{dry}	thermal conductivity at dried state, first used in Eq. (2)	f^Q	internal/external energy supply, first used in Eq. (6)
λ_{sat}	thermal conductivity at saturated state, first used in Eq. (2)	f^w	internal/external water supply, first used in Eq. (6)
λ	shape parameter for the retention curve, first used in Eq. (12)	\mathbf{g}	gravity acceleration, first used in Eq. (11)
λ_w	model parameter in Eq. 1, first used in Eq. (1)	G_s	soil density, first used in Eq. (1)
μ_l	dynamic viscosity of the pore liquid, first used in Eq. (11)	\mathbf{i}_c	energy flux due to conduction, first used in Eq. (6)
μ_o	model parameter for dynamic viscosity, first used in Eq. (14)	$\mathbf{J}_{E(\cdot)}$	advective flux of energy caused by mass motions, first used in Eq. (6)
μ_T	empirical coefficient of relative viscosity, first used in Eq. (1)	\mathbf{j}_g^w	mass motion of water in gas phase as the moisture, first used in Eq. (3)
∇^t	partial derivative operator at time t , first used in Eq. (28)	\mathbf{j}_l^w	mass motion of water in liquid phase, first used in Eq. (3)
ν	Poisson ratio, first used in Eq. (8)	\mathbf{k}	tensor permeability, first used in Eq. (1)
ω_g^w	vapor density, first used in Eq. (15)	k	time step in finite difference, first used in Eq. (22)
ϕ	porosity, first used in Eq. (3)	k_{rl}	relative permeability, first used in Eq. (11)
$\rho_{(\cdot)}$	density of (\cdot) phase i.e. gas, solid, liquid, first used in Eq. (6)	\mathbf{k}_o	the tensor of reference intrinsic permeability, first used in Eq. (1)
ρ_v	vapor density, first used in Eq. (15)	l	iteration step in Newton-Raphson, first used in Eq. (22)
$\boldsymbol{\sigma}$	stress tensor, first used in Eq. (5)	M_w	molecular mass of water, first used in Eq. (17)
τ	tortuosity, first used in Eq. (15)	N_i	shape function, first used in Eq. (26)
θ_g^w	volumetric mass of water in the gas phase, first used in Eq. (3)	P_g	gas pressure, first used in Eq. (9)
θ_l^w	volumetric mass of water in the liquid phase, first used in Eq. (3)	P_l	liquid pressure, first used in Eq. (9)
$\boldsymbol{\varepsilon}^{T-e}$	elastic strain induced by temperature, first used in Eq. (7)	P_o	parameter for retention curve, first used in Eq. (13)
$\boldsymbol{\varepsilon}^{\sigma-e}$	elastic strain induced by stress, first used in Eq. (7)	\mathbf{q}_l	vector flux of liquid phase, first used in Eq. (11)
$\boldsymbol{\varepsilon}^{s-e}$	elastic strain induced by suction, first used in Eq. (7)	$\mathbf{r}_{(\cdot)}$	residual vector of the field (\cdot) , first used in Eq. (22)
$\boldsymbol{\varepsilon}^e$	elastic strain, first used in Eq. (7)	s	suction/capillary pressure, first used in Eq. (10)
\mathbf{A}	represents the conductance matrix, first used in Eq. (33)	S_e	effective degree of saturation, first used in Eq. (12)
$\mathbf{a}_{(\cdot)}$	flux and conductance of the field (\cdot) , first used in Eq. (32)	S_g	gas degree of saturation, first used in Eq. (3)
\mathbf{b}	vector of body forces, first used in Eq. (5)	S_l	liquid degree of saturation, first used in Eq. (2)
\mathbf{B}	gradients of shape functions, first used in Eq. (19)	S_e	maximum liquid degree of saturation, first used in Eq. (13)
$\mathbf{b}_{(\cdot)}$	boundary conditions of the field (\cdot) , first used in Eq. (32)	S_{rl}	residual liquid degree of saturation, first used in Eq. (13)
b	model parameter for dynamic viscosity, first used in Eq. (14)	T	temperature, first used in Eq. (1)
$\mathbf{d}_{(\cdot)}$	storage or accumulation of the field (\cdot) , first used in Eq. (32)	t	time, first used in Eq. (3)
		\mathbf{u}	vector of displacement, first used in Eq. (21)
		w	water content, first used in Eq. (1)
		w_o	reference water content, first used in Eq. (1)
		\mathbf{X}	vector of unknowns, first used in Eq. (33)

solution of the system of equations using a combination of parallel computation (openMP), storage in Compressed Sparse Row format [13] and the iterative pre-conditioned Conjugate Gradient Squared method [14]. The results show that the computational cost decreases significantly.

Based on the coupled THM model, we performed numerical simulations for 3D problems applied to the Fürwigge dam. The transient displacement, temperature and water transport are validated with the measured data [2]. The results show that the numerical simulations have a good agreement with the data measured and can be assumed to be validated.

2. Phenomena and mechanisms in masonry dams

2.1. Stress and strain relations

The dam was built using rock blocks and mortar. There are two material patterns, the thin leaf has a regular pattern, whereas the infill has an irregular or random pattern. The elastic modulus of

rock is much higher than the elastic modulus of mortar. In meso-scale problem, heterogeneous material can be treated by representative volume elements under the light of first order homogenization theory [15]. However, within the scope of this study, the masonry material is considered as a homogeneous and isotropic material because of the given large scale problem and that major parts of the dam volume follow a random pattern. The stress-strain relations can be influenced by the temperature and wetness state of the masonry materials. The deformation may cause the change in porosity and thus cause the change in permeability, however, the change in porosity can be ignored in cases of the small deformation.

2.2. Effects of temperature

The temperatures inside the dam body and at the boundary are different. Furthermore, the temperature at the surfaces in contact with water are different from the surfaces in contact with air. Water temperature varies significantly with seasons at the water

surface, while it does not change significantly at the bottom location of the reservoir. The effects of temperature on the deformation have been quantified experimentally [1]. It shows that a change of $\pm 1^\circ\text{C}$ may cause 0.21 mm deformation at the dam crest of a dam 28 m high. As compared with the pressure of 26 m water column on the dam, which changes ± 1 m, may cause ± 0.61 mm deformation, the effect of temperature is significant. Thermal expansion of the materials has been known and monitored over long periods. The volumetric expansion of the material is quantified as a linear relation between temperature and volumetric strain.

The change of temperature in the dam body affects the infiltration process due to: (1) the change of viscosity of water and (2) the diffusion of water vapor from high-temperature zones to low-temperature zones. These phenomena have been measured and discussed in [16] and modeled in [17].

Effects of temperature on permeability have also been considered in previous studies. Push [18] observed an increase in the coefficient of permeability of bentonite MX-80 and Ca-bentonite according to Darcy's law when the temperature changed from 20°C to 70°C at a low hydraulic gradient. The effect of the temperature on the permeability of unsaturated media has been quantified as follows [19]:

$$\mathbf{k}(e, w, T) = \mathbf{k}_0(1 + \mu_T(T - T_0))10^{ae} \left(\frac{w - w_0}{e/G_s - w_0} \right)_w^\lambda, \quad (1)$$

where e/G_s is the saturated water content, w and w_0 are the water content and reference water content, μ_T is the empirical coefficient fitting of relative viscosity, a and λ_w are the model parameters, \mathbf{k}_0 is the reference intrinsic permeability, T is the temperature, T_0 is the reference temperature, e is the void ratio, and G_s is the soil density.

2.3. Effects of water infiltration

The water infiltration, on the other hand, affects the thermal conduction. The increase of water content in the mortar causes an increase in thermal conductivity and vice versa. The phenomenon has been quantified by the relation [20]:

$$\lambda_T = \lambda_{sat}^{S_l} \lambda_{dry}^{(1-S_l)}, \quad (2)$$

where λ_T is the thermal conductivity, λ_{sat} and λ_{dry} are the thermal conductivities in the saturated and dry state, respectively and S_l is the liquid saturation.

Water infiltration also affects the stress-strain relations of the material. It induces the volumetric expansion and shrinkage of the material. Expansion and shrinkage of the material depend on water saturation in the pores. This phenomenon has been observed and modeled by some authors, e.g. [21,22].

In summary, the effects of temperature on material behavior of the masonry dams have been characterized by their effects on stress-strain relations and their effects on pore-water transport. Conversely, the change of water content affects on the thermal conductivity and stress-strain relations. Therefore, it is necessary to simulate the masonry dam by means of fully coupled THM analysis. In the next section, the theoretical framework of multi-physics for THM modeling will be presented.

3. Theoretical framework for THM modeling

The THM problems are formulated by a system of balance equations. Equations for mass balance were established by following the compositional approach [23]. Constitutive equations are used to connect between the primary unknowns (i.e. displacements, liquid pressure, gas pressure and temperature) to the parameters and the dependent variables e.g. water saturation, energy flux and so on.

3.1. Balance equations

Mass balance of water: Water is present in the liquid and gas phases. In this paper, due to slow fluxes and low permeability we assume that gas pressure is constant and equal to zero. The total mass balance of water is expressed as follows:

$$\frac{\partial}{\partial t} (\theta_l^w S_l \phi + \theta_g^w S_g \phi) + \nabla \cdot (\mathbf{j}_l^w + \mathbf{j}_g^w) = f^w. \quad (3)$$

Assuming that the pores contain only gas and liquid, we consider the relation

$$S_g + S_l = 1, \quad (4)$$

where S_g is the degree of saturation of gas, ϕ is porosity, f^w is an external supply of water, and θ_l^w and θ_g^w are the volumetric mass of water in the liquid and gas phases, respectively. Moreover, \mathbf{j}_l^w is the total mass motion of water in liquid phase including non-advective (\mathbf{i}) and advective fluxes (\mathbf{q}), \mathbf{j}_g^w is a mass motion of water in the gas phase as the moisture.

Momentum balance for the medium: The momentum balance reduces to the equilibrium of stresses if the inertial terms are neglected as:

$$\nabla \cdot \boldsymbol{\sigma} + \mathbf{b} = \mathbf{0}, \quad (5)$$

where, $\boldsymbol{\sigma}$ is the stress tensor and \mathbf{b} is the vector of body forces.

Internal energy balance for the medium: The equation for the internal energy balance for the porous medium is established by taking into account the internal energy in each phase (E_s, E_l, E_g) as:

$$\frac{\partial}{\partial t} (E_s \rho_s (1 - \phi) + E_l \rho_l S_l \phi + E_g \rho_g S_g \phi) + \nabla \cdot (\mathbf{i}_c + \mathbf{j}_{Es} + \mathbf{j}_{El} + \mathbf{j}_{Eg}) = f^Q, \quad (6)$$

where, \mathbf{i}_c is the energy flux due to the conduction through the porous medium, the fluxes \mathbf{j}_{Es} , \mathbf{j}_{El} and \mathbf{j}_{Eg} are advective fluxes of energy caused by mass motions and f^Q is an internal/external energy supply, ρ_s is the density of solid, ρ_l is the density of the liquid, and ρ_g is the density of gas.

3.2. Constitutive relations

The final objective is to find the unknowns from the balance equations. Therefore, the dependent variables have to be related to the unknowns in the following constitutive relations.

3.2.1. Thermo-elastic model for stress-strain relations

The mechanical constitutive equation takes the incremental general form. The elastic part of the strain increment is a sum of the increments of suction induced $d\boldsymbol{\varepsilon}^{s-e}$, effective stress induced $d\boldsymbol{\varepsilon}^{\sigma-e}$, and the strain increment due to temperature change $d\boldsymbol{\varepsilon}^{T-e}$. The final relation for the elastic strain increment is

$$d\boldsymbol{\varepsilon}^e = d\boldsymbol{\varepsilon}^{\sigma-e} + d\boldsymbol{\varepsilon}^{s-e} + d\boldsymbol{\varepsilon}^{T-e}. \quad (7)$$

The elastic strain is described according to Hooke's law as:

$$d\boldsymbol{\varepsilon}^{\sigma-e} = \begin{pmatrix} \varepsilon_{xx} \\ \varepsilon_{yy} \\ \varepsilon_{zz} \\ \tau_{xy} \\ \tau_{xz} \\ \tau_{yz} \end{pmatrix}^{\sigma-e} = (\mathbf{D}^e)^{-1} \begin{pmatrix} \sigma'_{xx} \\ \sigma'_{yy} \\ \sigma'_{zz} \\ \gamma'_{xy} \\ \gamma'_{xz} \\ \gamma'_{yz} \end{pmatrix} = (\mathbf{D}^e)^{-1} d\boldsymbol{\sigma}', \quad (8)$$

where \mathbf{D}^e is the elastic material matrix of the solid phase defined by the elastic modulus (E) and Poisson ratio (ν). For isotropic materials, \mathbf{D}^e can be written as $\mathbf{D}^e = \lambda \mathbf{I} \otimes \mathbf{I} + 2\mu \mathbf{I}$ where λ and μ are the Lamé constants. The effective stress tensor $\boldsymbol{\sigma}'$ is defined as

$$\boldsymbol{\sigma}' = \boldsymbol{\sigma} - \max(P_g, P_l)\boldsymbol{\delta}, \quad (9)$$

where $\boldsymbol{\sigma}$ is the total stress tensor, P_g is the gas pressure and P_l is the liquid pressure, $\boldsymbol{\delta}$ is Kronecker's tensor. This means $\boldsymbol{\sigma}'$ is a net stress in the unsaturated state and an effective stress in the saturated state.

According to [1,22] the changes of capillary pressure and temperature cause the expansion and shrinkage of masonry materials. Herein, suction and temperature induce only volumetric strains with constitutive equations given as follows

$$d\boldsymbol{\varepsilon}^{s-e} = 3\alpha_s ds \quad \text{and} \quad d\boldsymbol{\varepsilon}^{T-e} = 3\alpha_T dT, \quad (10)$$

where $s = (P_g - P_l) \geq 0$ is suction or capillary pressure, α_T is the coefficient of thermal expansion, α_s is coefficient of swelling/shrinkage induced by suction. The first equation is valid when suction is greater than or equal to zero.

3.2.2. Constitutive model for water transport

Advective flow of the water phase is described by the generalized Darcy's law for hydraulic processes:

$$\mathbf{q}_l = -\frac{\mathbf{k}_o k_{rl}}{\mu_l} (\nabla \cdot P_l - \rho_l \mathbf{g}), \quad (11)$$

where μ_l is the dynamic viscosity of the pore liquid, \mathbf{g} is the gravity acceleration, ρ_l is the liquid density and $\mathbf{k}_o = \text{diag}(k_{ox}, k_{oy}, k_{oz})$ is the tensor of reference intrinsic permeability, assuming that the material is isotropic, \mathbf{k}_o is described by solely one permeability value k_o .

The relative permeability k_{rl} , is derived from Mualem-van Genuchten closed form model, [24,25]:

$$k_{rl} = \sqrt{S_e} \left(1 - \left(1 - S_e^{1/\lambda} \right)^\lambda \right)^2, \quad (12)$$

where λ is a shape parameter for the retention curve and an effective degree of saturation S_e is defined as:

$$S_e = \frac{S_l - S_{rl}}{S_l - S_{rl}} = \left(1 + \left(\frac{P_g - P_l}{P_o} \right)^{1/\lambda} \right)^{-\lambda}, \quad (13)$$

where S_l , S_{ls} and S_{rl} are the current, the maximum and the residual liquid degree of saturation, respectively; P_o is a model parameter.

The dynamic water viscosity depends on temperature empirically provided by [26] according to the following formula:

$$\mu_l = \mu_0 \exp\left(\frac{b}{273.15 + T}\right), \quad (14)$$

where μ_0 and b are the model parameters.

Molecular diffusion of vapor in the air is governed by Fick's law. The diffusion coefficient is m^2/s ; Fick's law is adopted to define the diffusive flux of the water vapor \mathbf{i}^v :

$$\mathbf{i}^v = -(\phi \rho_v S_l \tau D_m \mathbf{I}) \nabla \omega_g^w, \quad (15)$$

where ρ_v is the vapor density, ω_g^w is the mass fraction of the vapor, \mathbf{I} is the identity matrix, τ is the tortuosity and D_m , the diffusion coefficient of the vapor in m^2/s , is defined as:

$$D_m = D \frac{(273.15 + T)^{2.3}}{P_g}, \quad (16)$$

where D is the molecular diffusion coefficient at temperature 273.15 K.

The volumetric mass of vapor (Eq. (3)) is computed implicitly by the psychrometric law from the fraction of water phase according to [27]. The law describes the change of volumetric vapor density in the gas phase due to the curvature of the surface of water and temperature T ($^\circ\text{C}$)

$$\theta_g^w = (\theta_g^w)^0 \exp\left(\frac{-SM_\omega}{R(273.15 + T)\rho_l}\right), \quad (17)$$

where M_ω is a molecular mass of water, $(\theta_g^w)^0$ is a reference density of water vapor at $T = 0$ $^\circ\text{C}$, R is a universal gas constant water vapor (i.e. $8.31432 \text{ J mol}^{-1} \text{ K}^{-1}$). The volumetric mass of water in gas phase is a product of the mass fraction of water (ω_g^w) and bulk density of the water phase ρ_v i.e. $\theta_g^w = \omega_g^w \rho_v$.

3.2.3. Constitutive model for heat conduction

Fourier's law was adopted for the heat conduction flux, \mathbf{i}_c , of heat:

$$\mathbf{i}_c = -\lambda_T \nabla T \quad \text{where} \quad \lambda_T = \lambda_{sat}^{\lambda_T} \lambda_{dry}^{(1-\lambda_T)}, \quad (18)$$

where λ_T is the thermal conductivity, λ_{sat} and λ_{dry} are thermal conductivity in the saturated and dry state, respectively.

4. Numerical procedure

The system of Partial Differential Equations is solved numerically by Finite Element (FE) method where the systems of equations are solved either by LU factorization or by iterative Conjugate Gradient Squared method. The numerical analysis is composed by two terms: spatial and temporal discretization. The FE method is used to solve in spatial discretization in each time step. Because the problem presented here is temporally non-linear, the Newton-Raphson's method is applied. To solve the time dependency, finite difference schemes are applied, see Eq. (33). The FE approach introduced here is based on the formulations in Olivella et al. [23], Zienkiewicz et al. [28], and Milly [29].

4.1. Approach for stress equilibrium equations

The weighted residual method is applied to the stress equilibrium Eq. (5) followed by Green's theorem. This leads to the following equation, [28]

$$\mathbf{r}(\boldsymbol{\sigma}^{k+1}) = \int_{\Omega} \mathbf{B}^T \boldsymbol{\sigma}^{k+1} d\Omega - \mathbf{f}^{k+1}, \quad (19)$$

where $\mathbf{r}(\boldsymbol{\sigma}^{k+1})$ presents the residual vectors corresponding to the stress-strain problem, $\boldsymbol{\sigma}^{k+1}$ is the stress vector, the matrix \mathbf{B} is composed by gradients of shape functions and defined in such way that the stress is a vector, \mathbf{f}^{k+1} includes body force terms and boundary force terms. The strain related to the stress, fluid pressure, and temperature are defined by constitutive stress-strain relations in the temporal discretization form as:

$$\frac{d\boldsymbol{\varepsilon}}{dt} = (\mathbf{D}^e)^{-1} \frac{d\boldsymbol{\sigma}'}{dt} + \mathbf{m}\alpha_s \frac{ds}{dt} + \mathbf{m}\alpha_T \frac{dT}{dt}, \quad (20)$$

where α_s and α_T are coefficients for volumetric elastic expansion, \mathbf{m} is the an auxiliary vector $\mathbf{m}^T = (1, 1, 1, 0, 0, 0)$. Substituting the displacement in the Eq. (20) by $\boldsymbol{\varepsilon} = \mathbf{B}\mathbf{u}$, the Eq. (20) must be satisfied at every node in the domain Ω in terms of \mathbf{u} . Therefore, spatial and temporal discretizations lead to

$$\mathbf{h}^{k+1} = \delta^k(\boldsymbol{\sigma}) - \mathbf{D}^e \mathbf{B}_j \delta^k(\mathbf{u})_j + \mathbf{D}^e \mathbf{m} \mathbf{N}_j \alpha_s \cdot \delta^k(s)_j + \mathbf{D}^e \mathbf{m} \mathbf{N}_j \alpha_T \delta^k(T)_j \equiv \mathbf{0}, \quad (21)$$

where $\delta(\cdot) = (\cdot)^{k+1} - (\cdot)^k$ denotes the difference between two iteration values of the terms (\cdot) . Further \mathbf{h} contains the residual stresses

at every node, j indicates the summation over element nodes, N_j is a shape function of the element j . In each node of the domain Ω the Eq. (21) must vanish so that the material behavior obeys the constitutive laws. If the stress in Eq. (21) could be obtained explicitly, we can substitute Eq. (21) in Eq. (19) and compute the residuals. However, these models are temporal non-linear models. Therefore, an iterative Newton-Raphson's method is applied. Herein, for finding the solution for the time step t^{k+1} , the Newton-Raphson iteration have to be carried out l times and the unknowns are written as $(\cdot)^{l+1}$ instead of $(\cdot)^{k+1,l+1}$. From Eq. (19), applying a Taylor expansion of the residual, we obtain:

$$\mathbf{r}^{l+1} = \mathbf{r}^l + \int_{\Omega} \mathbf{B}^T \delta^l(\boldsymbol{\sigma}) d\Omega, \tag{22}$$

where $\delta(\cdot) = (\cdot)^{l+1} - (\cdot)^l$ denotes the difference between two Newton-Raphson iteration values of the terms (\cdot) .

Having equality in Eq. (21), we obtain the following equation which needs to be solved during each iteration step:

$$\mathbf{h}^{l+1} = \mathbf{h}^l + \frac{\partial \mathbf{h}^l}{\partial \boldsymbol{\sigma}} \delta^l(\boldsymbol{\sigma}) + \frac{\partial \mathbf{h}^l}{\partial \mathbf{u}} \delta^l(\mathbf{u}) + \frac{\partial \mathbf{h}^l}{\partial S} \delta^l(P_l) + \frac{\partial \mathbf{h}^l}{\partial T} \delta^l(T). \tag{23}$$

Considering $\partial \mathbf{h}^l / \partial \mathbf{u} = \mathbf{B}$, substitution Eq. (23) to Eq. (22) we obtain the equation regarding stress equilibrium.

$$\int_{\Omega} \mathbf{B}^T \mathbf{D}^e \mathbf{B}_j \delta^l(\mathbf{u}) d\Omega + \int_{\Omega} \mathbf{B}^T \mathbf{D}^e \frac{\partial \mathbf{h}^l}{\partial S} \delta^l(S) d\Omega + \int_{\Omega} \mathbf{B}^T \mathbf{D}^e \frac{\partial \mathbf{h}^l}{\partial T} \delta^l(T) d\Omega = -\mathbf{r}^l - \int_{\Omega} \mathbf{B}^T \mathbf{D}^e \mathbf{h}^l d\Omega. \tag{24}$$

In the Eq. (24) the right-hand side is known from the previous iteration, the left-hand side, after expanding derivatives, can be expressed as a function of three unknowns: \mathbf{u} , P_l , and T . This equation is solved simultaneously with the other equations (mass and energy balance equations).

4.2. Approach for mass and energy balance equations

In this present study, the terms presented in mass and energy balance equations are storage terms, advective fluxes, and non-advective fluxes. In order to explain the approach for the different equations some basic notations are introduced. The notation i represents the i -th node in a finite element mesh, e_1, e_2, \dots, e_m are the elements containing node i , n_{e_m} is the number of nodes in element e_m (e.g. $n_{e_m} = 3$ for triangle element, $n_{e_m} = 4$ for tetrahedron element), Ω_{e_m} is the volume of element e_m , N_i is the shape function for node i .

4.2.1. Approach for storage terms

Masonry materials are characterized by a high elastic modulus and small deformations. Therefore, we consider a constant porosity under the loads. The Eq. (3) can be rewritten as:

$$\phi \frac{\partial}{\partial t} (\theta_l^w S_l + \theta_g^w S_g) + \nabla \cdot (\mathbf{j}_l^w + \mathbf{j}_g^w) = f^w. \tag{25}$$

The final objective is to find the unknown P_l from the governing equation. Hence, the dependent variables S_l and S_g will be computed using the retention curve [Eq. (13)]. The mass conservation in time is achieved if the time derivatives are directly approximated by finite differences in time. The finite element method for space discretization conserves mass as presented in [29]. The weighted residual method is applied to the balance equations, therefore the first term of Eq. (25), which relates to liquid saturation is transformed as:

$$\int_{\Omega} N_i \phi \frac{\partial (\theta_l^w S_l)}{\partial t} d\Omega = \int_{e_1} N_i \phi \frac{\partial (\theta_l^w S_l)}{\partial t} d\Omega + \dots + \int_{e_m} N_i \phi \frac{\partial (\theta_l^w S_l)}{\partial t} d\Omega. \tag{26}$$

Using approximations for temporal finite differences at time step k , we obtain a formula for every integral, for example, for the first element:

$$\int_{e_1} N_i \phi \frac{\partial (\theta_l^w S_l)}{\partial t} d\Omega = \phi_{e_1}^k \left(\frac{(\theta_l^w S_l)_{i,e_1}^{k+1} - (\theta_l^w S_l)_{i,e_1}^k}{t^{k+1} - t^k} \right) \int_{e_1} N_i d\Omega. \tag{27}$$

This approximation allows us to make the space integration independent from the physical variables. Consequently, the computation of the geometrical coefficients is necessary only once for a given finite element mesh.

4.2.2. Approach for advective terms

The weighted residual method is applied to the balance equation. After that, Green's theorem is applied to reduce the order of the derivatives and the divergence of flows is transformed into two terms. Using Darcy's law, this can be written at node i as follows:

$$-\int_{\Omega} \nabla^t N_i \theta_l^w \mathbf{q}_l d\Omega = \left(\int_{\Omega} \nabla^t N_i \theta_l^w \frac{\mathbf{k} \mathbf{k}_{rl}}{\mu_l} \nabla N_j d\Omega \right) (P_l)_j - \int_{\Omega} \nabla^t N_i \theta_l^w \frac{\mathbf{k} \mathbf{k}_{rl}}{\mu_l} \rho_l \mathbf{g} d\Omega, \tag{28}$$

where j denotes the summation over the element nodes, $(P_l)_j$ is node-wise variable, where its values are defined by nodes and interpolation over nodes by means of shape functions.

For the node i the volume Ω over which the integral in Eq. (28) has to be performed in the composition of the elements e_1, e_2, \dots, e_m . The contribution of element e_m to the total lateral flux towards node i is approximated as:

$$\left(\int_{\Omega} \nabla^t N_i \theta_l^w \frac{\mathbf{k} \mathbf{k}_{rl}}{\mu_l} \nabla N_j d\Omega \right) (P_l)_j \approx \mathbf{k} \left(\theta_l^w \frac{\mathbf{k}_{rl}}{\mu_l} \right)_{e_m}^{k+\varepsilon} \left(\int_{e_m} \nabla^t N_i \nabla N_j d\Omega \right) (P_l)_j^{k+\theta}, \tag{29}$$

where two different intermediate points are used: $(k + \theta)$ is used for pressure, and $(k + \varepsilon)$ for the relative permeability. The integrals of products of the shape function gradient are considered as the influence coefficients. They have to be computed for each element but only once for a given mesh.

A similar approximation is applied for the gravity term in Eq. (28). The evaluation of density element-wise is convenient in order to balance correctly the pressure gradients with the gravity forces at the element level.

4.2.3. Approach for non-advective terms

In the balance equation of node i , we have the following diffusion term:

$$-\int_{\Omega} \nabla^t N_i \mathbf{i}_l^w d\Omega = \left(\int_{\Omega} \nabla^t N_i \phi \tau \rho_l S_l D_m \mathbf{I} \nabla N_j d\Omega \right) (\omega_l^w)_j, \tag{30}$$

where ω_l^w is considered a node-wise variable, subscript j denotes the summations over the nodes of an element j , the other notations are explained after Eq. (15). The contribution of element e_m to the total lateral flux towards node i is approximated as:

$$\left(\int_{\Omega} \nabla^t N_i \phi \tau \rho_l S_l D_m \mathbf{I} \nabla N_j d\Omega \right) (\omega_l^w)_j = (\phi \tau)_{e_m}^k (\rho_l S_l D_m)_{e_m}^{k+\varepsilon} \left(\int_{e_m} \nabla^t N_i \mathbf{I} \nabla N_j d\Omega \right) (\omega_l^w)_j^{k+\theta}, \tag{31}$$

where the intermediate points are used similarly to the advective terms. The integral part can be computed just once for a given mesh.

4.3. System of balance equations

After the spatial discretization of the PDEs is established, the residuals that are obtained may be written as:

$$\begin{pmatrix} \mathbf{r}_u \\ \mathbf{r}_{p_l} \\ \mathbf{r}_T \end{pmatrix} = \frac{d}{dt} \begin{pmatrix} \mathbf{d}_u \\ \mathbf{d}_{p_l} \\ \mathbf{d}_T \end{pmatrix} + \begin{pmatrix} \mathbf{a}_u \\ \mathbf{a}_{p_l} \\ \mathbf{a}_T \end{pmatrix} + \begin{pmatrix} \mathbf{b}_u \\ \mathbf{b}_{p_l} \\ \mathbf{b}_T \end{pmatrix} \equiv 0, \quad (32)$$

where $\mathbf{r}_{(\cdot)}$ is the residual, $\mathbf{d}_{(\cdot)}$ is the storage or accumulation term, $\mathbf{a}_{(\cdot)}$ relates to both the advective and non-advective fluxes, it can be referred to the conductance term, $\mathbf{b}_{(\cdot)}$ includes boundary conditions. In time discretization the Eq. (32) may be written as:

$$\mathbf{r}(\mathbf{X}^{k+1}) = \frac{\mathbf{d}^{k+1} - \mathbf{d}^k}{\Delta t^k} + \mathbf{A}(\mathbf{X}^{t+\varepsilon}, \mathbf{X}^{t+\theta}) + \mathbf{b}(\mathbf{X}^{t+\varepsilon}, \mathbf{X}^{t+\theta}) \equiv 0, \quad (33)$$

where k is the time step index, \mathbf{X} is the vector of unknowns per node,

$\mathbf{X} = \{(u_x, u_y, u_z, P_l, T)_1, (u_x, u_y, u_z, P_l, T)_2, \dots, (u_x, u_y, u_z, P_l, T)_n\}$, \mathbf{A} represents the conductance matrix. The Newton-Raphson's scheme for this non-linear system of balance equation is written as:

$$\frac{\partial \mathbf{r}(\mathbf{X}^{k+1})}{\partial \mathbf{X}^{k+1}} (\mathbf{X}^{k+1,l+1} - \mathbf{X}^{k+1,l}) \equiv -\mathbf{R}(\mathbf{X}^{k+1,l}), \quad (34)$$

where l denotes the number of iterations. The residual error estimation can be verified by estimation methods [30].

4.4. Solution of the system of equations

Conventionally, the LU factorization method is used as a solver for the system of equations and band storage format is used as data storage. However, the band storage format requires a large amount of memory, especially, when the degrees of freedom in the nodes and the number of elements increase. In this project, we use Compressed Sparse Row format (CSR) [13] to store the matrix, in which only non-zero elements are stored. This method allows increasing the storage capacity as well as increasing speed of data accessing.

Direct LU factorization is computationally expensive when solving large sparse non-symmetric matrices. One of the effective algorithms for such procedures is pre-conditioned Conjugate Gradient Squared method (CGS) [14]. This iterative method is a modification of Conjugate Gradient method in order to solve non-symmetric matrices. The method requires extra space and pre-conditioners. The pre-conditioning matrix is used in order to accelerate the rate of convergence. However, using CRS format plus CGS iterative solution with parallel block-diagonal inversion has a simple structure. The CGS algorithm is described in Algorithm 1. A series of computational tests is performed in a coupled 3-dimensional THM problem for comparing LU factorization using band storage format with iterative CGS method using CRS format. For the tests, different discretizations are generated from coarse to fine meshes in the same geometry.

Furthermore, in order to increase the speed of computations, we solved the system of equations with multi-threading techniques with a cluster computer. The iterative CRS + CGS method was used as a computational test. We used OpenMP library to distribute the jobs among different processors for the inversion and multiplication of the matrices according to Algorithm 1. A fine mesh with more than 94 thousand tetrahedral elements was selected for these tests. The numerical simulation was implemented in Code_bright FE code. The comparison and discussion are presented in the result section.

Algorithm 1. Conjugate Gradient Squared algorithms after modified [23].

Precondition:

- | | |
|--------------------------------------------------------------------------------------------------------|------------------------------------------------------|
| 1: $\mathbf{x} := \mathbf{x}_0$ | ▷ initial guess |
| 2: $\mathbf{r} := \mathbf{b} - \mathbf{A}\mathbf{x}$ | ▷ \mathbf{r} is the residual vector |
| 3: $\tilde{\mathbf{r}}$ is an arbitrary vector such that $(\mathbf{r}, \tilde{\mathbf{r}}) \neq 0$ | |
| 4: $\rho_0 = (\mathbf{r}, \tilde{\mathbf{r}}); \beta_0 = \rho_0; \mathbf{p} = \mathbf{q} = \mathbf{0}$ | ▷ \mathbf{p}, \mathbf{q} are the auxiliary vectors |
| 5: \mathbf{K} is pre-conditioner matrix (diagonal of \mathbf{A}) | |
| 6: procedure CONJUGATE GRADIENT SQUARED ITERATION | |
| 7: for $i \leftarrow 1$ to n do | |
| 8: $\mathbf{u} := \mathbf{r} + \beta_i \mathbf{q}$ | |
| 9: $\mathbf{p} := \mathbf{u} + \beta_i (\mathbf{q} + \beta_i \mathbf{p})$ | |
| 10: Solve \mathbf{q} from $\mathbf{K}\mathbf{q} = \mathbf{p}$ | ▷ invert matrix with OpenMP |
| 11: $\mathbf{v} := \mathbf{A}\mathbf{q}$ | ▷ matrix × vector with OpenMP |
| 12: $\alpha_i = \rho_i / (\tilde{\mathbf{r}}, \mathbf{v})$ | |
| 13: $\mathbf{q} := \mathbf{u} - \alpha_i \mathbf{v}$ | |
| 14: Solve \mathbf{v} from $\mathbf{K}\mathbf{v} = \mathbf{u} + \mathbf{q}$ | ▷ invert matrix with OpenMP |
| 15: $\mathbf{u} := \mathbf{A}\mathbf{v}$ | ▷ matrix × vector with OpenMP |
| 16: $\mathbf{x} := \mathbf{x} + \alpha_i \mathbf{v}$ | |
| 17: $\mathbf{r} := \mathbf{r} + \alpha_i \mathbf{u}$ | |
| 18: if $(\mathbf{r} < \varepsilon)$ then | ▷ ε is the convergence criterion |
| 19: return (\mathbf{x}) | |
| 20: else | |
| 21: $\rho_{i+1} = (\mathbf{r}, \tilde{\mathbf{r}})$ | |
| 22: $\beta_{i+1} = \rho_{i+1} / \rho_i$ | |
| 23: end if | |
| 24: end for | |
| 25: end procedure | |
-

5. Parameters, boundary, and initial conditions

5.1. Parameters

Parameters used in numerical simulations are given by literature on the Fürwigge Dam and similar masonry dams in Germany. The parameters may be calibrated afterwards to fit with particular conditions of the dam. The parameters for stress-strain behavior and Darcy's law are provided in the literature [2]. The parameters for general materials like water and solid density are provided by the handbook [26]. The parameters for diffusion are based on [31]. Other parameters, which are not found in the literature, are empirically assumed based on the experimental data of similar materials. The input parameters are presented in Table 1.

It was observed that viscosity changes with respect to the change of the chemical composition of water. With the change of pH value and water's hardness the viscosity of water is also changed. Based on the literature, the viscosity of the water in Eq. (14) is studied in two cases: (1) pure water $\mu_0 = 2.1 \times 10^{-12}$ MPa s and $b = 1808.5$ K, (2) reservoir water $\mu_0 = 2.5 \times 10^{-12}$ MPa s and $b = 2000$ K.

Table 1
Model parameters.

E	ν	ϕ_o	α_f	α_s	k_o	μ_o	P_o
GPa	–	–	$^{\circ}\text{C}^{-1}$	MPa^{-1}	m^2	MPa s	MPa
3.2	0.22	0.14	6.0E-06	–1.0E-07	2.1E-14	2.1E-12	0.001
λ	S_{rl}	S_{ls}	λ_{dry}	λ_{sat}	τ	D	ρ_s
–	–	–	Wm K^{-1}	Wm K^{-1}	–	$\text{m}^2\text{Pa/s K}^n$	kg m^{-3}
0.556	0.09	1	0.6	3.32	0.8	5.90E-06	2750

5.2. Boundary and initial conditions

For force and displacement boundary conditions, a combination of Neumann type and Cauchy type boundary conditions are used as:

$$f_x = f_x^o + \gamma(\dot{u}_x^o - \dot{u}_x) \tag{35}$$

$$f_y = f_y^o + \gamma(\dot{u}_y^o - \dot{u}_y) \tag{36}$$

$$f_z = f_z^o + \gamma(\dot{u}_z^o - \dot{u}_z), \tag{37}$$

where $f(\cdot)$ is the force in the (\cdot) direction, \dot{u}^o is the displacement rate, a very large value of γ can be used to impose a fixed displacement rate. For the simulation of the Fürwigge dam, we assume that the bedrock is very stiff, therefore, the nodes at the interfaces between the dam and the bedrock are fixed as: $\dot{u}_x^o = \dot{u}_y^o = \dot{u}_z^o = 0$. For the flux boundary conditions, the boundary conditions are incorporated by means of the simple addition of nodal flow rates. For instance, the mass flow rate of water, as a component vapor in unsaturated materials, is:

$$j_l^w = (\omega_l^w)^o j_l^o + \gamma_l (\omega_l^w)^o (P_l^o - P_l), \tag{38}$$

where the superscript $(\cdot)^o$ stands for prescribed values, γ_l is a leakage coefficient, P_l^o is the liquid pressure on the node. For the Fürwigge dam case, we modeled a drainage system as lines as in Fig. 1, P_l^o is applied on the nodes at the upstream side boundaries of the dam and also at the drainage lines. The development of the water column is presented in Fig. 2. In each time step, the boundary nodes at the upstream side are loaded with the forces and the water pressures interpolated from the water head as described in this figure. The nodes on the drainage lines begin to get the water pressure $P_l^o = 0$ MPa at the time step equal to 22 days, when infiltrating water meets the drainage lines.

For the energy balance equation, boundary conditions have the general form:

$$j_e = j_e^o + \gamma_e (T^o - T) + E_l^w (j_l^w) + E_l^a (j_l^a), \tag{39}$$

where the first term is a Neumann type prescribed energy inflow or outflow. The second term is a Cauchy boundary condition which

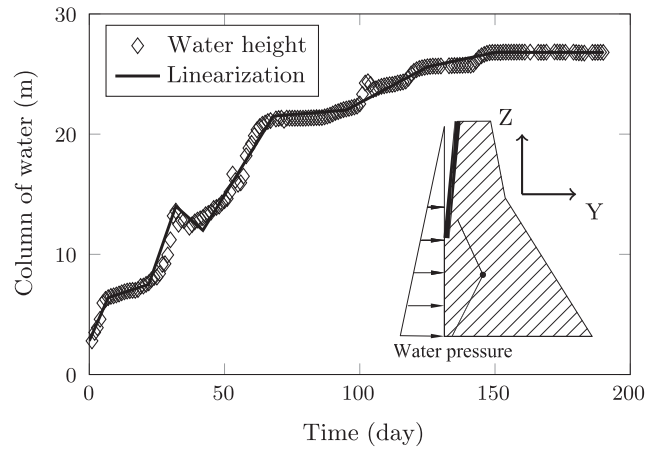


Fig. 2. Water level at upstream side.

may be used to prescribe temperature. The other terms are energy fluxes induced by the boundary conditions for the mass of liquid in term of water and vapor in the air phase a .

For the Fürwigge dam study, T^o is assigned to the nodes on the upstream side and the downstream side. Whenever the nodes are submerged in water, they will get the temperature as in Fig. 3 with the submerged time, otherwise, they will get weather temperature as in Fig. 4. The measurement locations (T1-T7) were placed not at the surface as in Fig. 3 but inside and near surface along the dam body. However, we assume that the temperature measured represents boundary temperature at the same height. T1-T7 locate at cross section A-A, the distances of measurement points (T1-T7) to the top of the dam are 2, 6, 10, 14, 18, 22, and 26 m, respectively. At the downstream side, the temperature boundary conditions applied on the node is also time-dependent as described in Fig. 4, where linear lines represent the mean values of measured air temperature.

In fact, the values of initial conditions (prior impounding process) like temperature, liquid pressure, and stress are not uniform over the

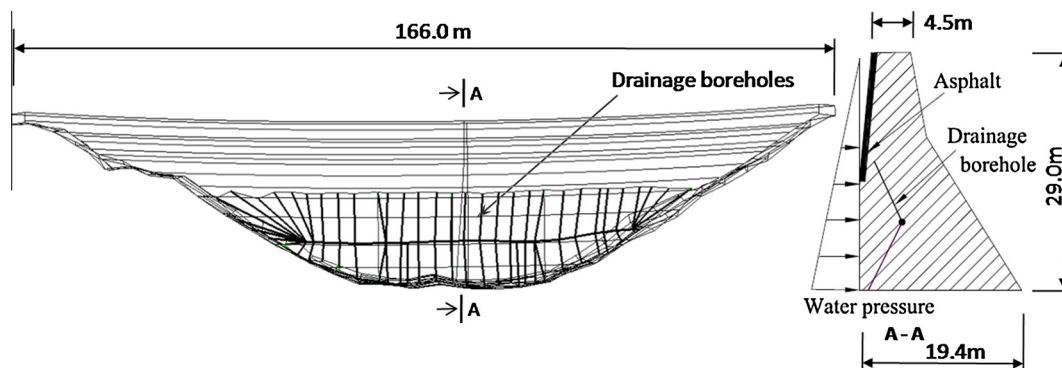


Fig. 1. Geometry – modeling of a new constructed drainage system.

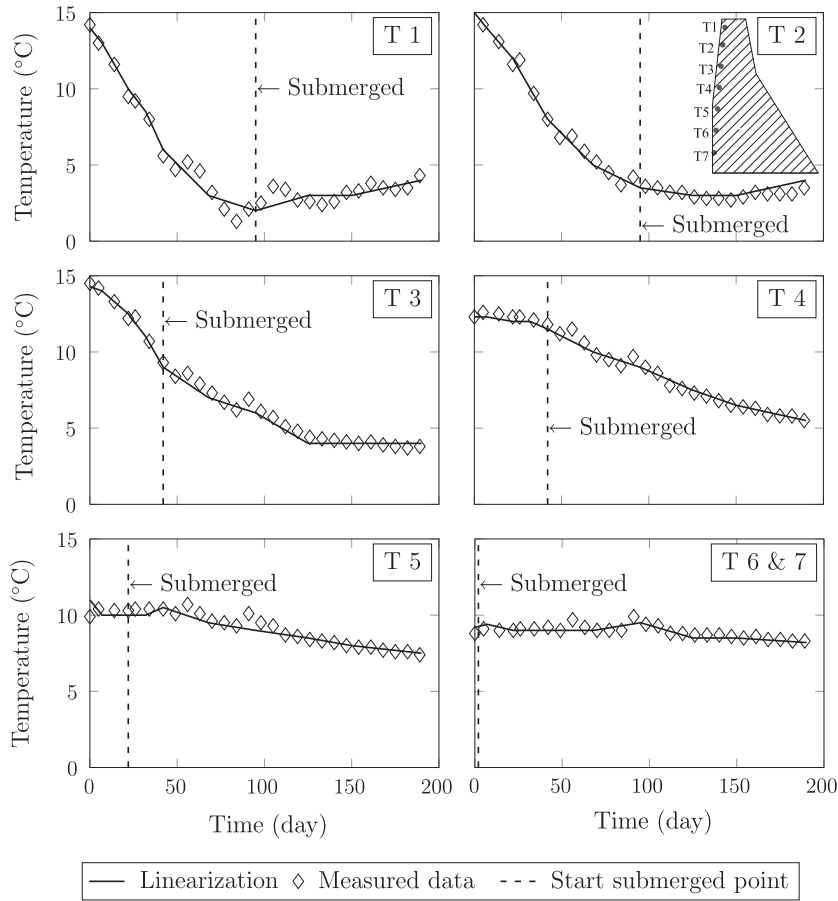


Fig. 3. Temperature at upstream side boundaries.

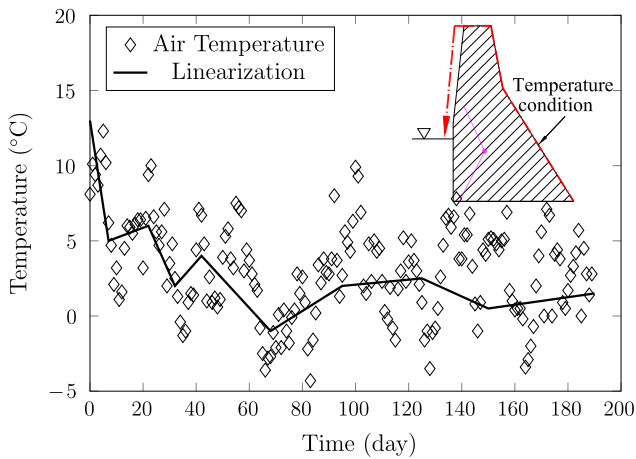


Fig. 4. Temperature at emerged boundaries.

whole dam volume. The distribution of the temperature in the structure is complex and depends on the highly changing annual ambient temperature. Therefore, based on measurement data at some locations, the initial conditions are assumed to be uniformly distributed as follows: $P_0 = -1.5$ kPa, $T_0 = 11.6$ °C and $\sigma_0 = 0$ kPa.

6. Geometry and discretization

Fürwigge dam is located at the south of Lüdenscheid, Germany. The dam is about 29 m high and 166 m long. The original drainage system of the dam was constructed behind the asphalt layer to collect the water infiltrating, however this drainage system got blocked and became non-functional after 100 years of usage. A drainage system plays an important role in the dam's safety as it decreases water pressure and water flux, hence, it prevents the masonry material from erosion and weathering processes. For extending the lifetime of the dam, new tunnels and a drainage system were constructed, see Figs. 5 and 6. Constructing the

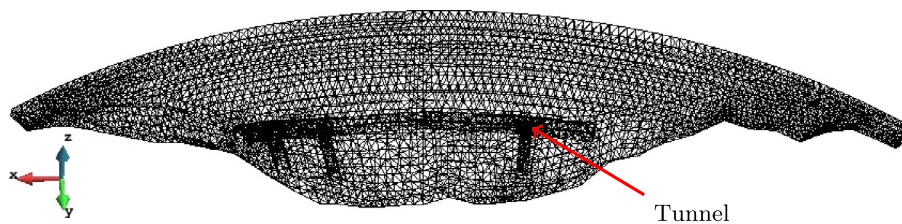


Fig. 5. Geometry – boundary discretization for the model with tunnels.

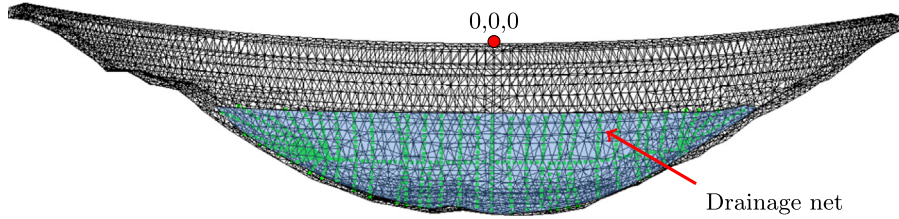


Fig. 6. Geometry – boundary discretization for the model with drainage system.

additional tunnels in the dam body may affect the strength of the dam. Furthermore, the efficiency of the drainage system must be assessed. However, modeling the tunnel and the boreholes as exactly as real geometrical volume requires a very fine mesh, which lead to very high computational cost. Therefore, we assess the serviceability of the new-built system considering two separate models:

1. To investigate the effects of technical tunnels on the displacement and stress-strain behavior, we develop a geometrical model including the exact volume of technical tunnels (see Fig. 5). The drainage system is ignored.
2. To assess the efficiency of the drainage boreholes system, the volumes of the tunnels and the boreholes is simplified to line elements (see Figs. 1 and 6). The effect of the tunnels in terms of stress-strain relations is ignored.

These two models support each other in order to have a better view on the impact of new-built system to the ordinary operation of the dam structure.

7. Results and discussions

7.1. Comparison of solution methods

The computational costs are presented in Fig. 7. The iterative CRS + CGS method performs much more effective when the number of 3D elements increases. It accelerates the computational process faster than 500 times when the number of elements is more than 50 thousand elements (see speedup curve in Fig. 7). In time-dependent problem, the CRS + CGS method improves the computational cost due to the usage of the pre-conditioned matrix and the initial guess x_0 which is based on the previous iteration step in Newton-Raphson’s method, while the LU method requires the same computational cost in every step.

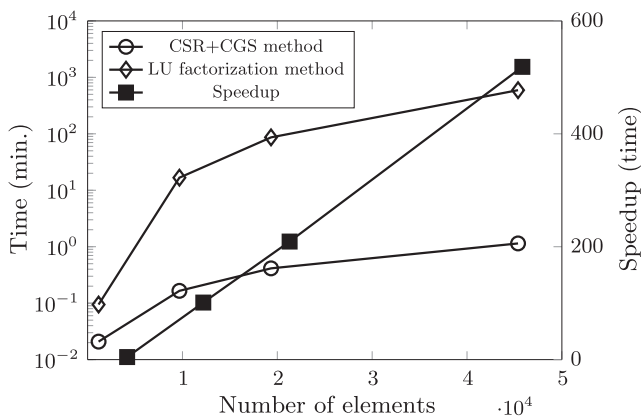


Fig. 7. Computational time between LU factorization and CSR + CGS.

The computational costs using parallel computations with multi-threading are presented in Fig. 8. The computational costs are normalized by dividing the solving time by the maximum solving time for each matrix A . This computational cost includes the cost of reading, updating, and writing data in iterative computations. The average of computational cost for different matrices are computed for each number of CPUs. The Fig. 8 shows that the computational time reduces slowly when the number of CPUs is more than 8 CPUs. The solving time decreases monotonically up to 5 times when increasing the number of CPUs. Therefore, we recommend to solve the 3D THM problems with 8 processors.

7.2. Fürwigge dam case

Six scenarios are studied in this paper:

1. The first case (THM simulation) is a standard case. In this case, we simulated a drainage net of the borehole in the dam body. The fully thermo-hydro-mechanical model is considered under non-isothermal boundary conditions. Viscosity for pure water is given. The asphalt layer as in Fig. 1 is considered non-functional. That means water is allowed to permeate into the dam from this area.
2. The second case (THM simulation & visco), a viscosity of impure water is considered as presented in Section 5.1.
3. In the third case (THM simulation & asphalt), the model is computed considering the functionality of asphalt layer. With the asphalt layer, water is not allowed to permeate into the dam body from this area.
4. In the fourth case (THM simulation & tunnel), the model is computed considering the technical tunnel in the dam body.
5. In the fifth case (HM simulation), the model is computed considering iso-thermal conditions. This case aims to quantify the separated effects of the temperature on the behavior of the dam.

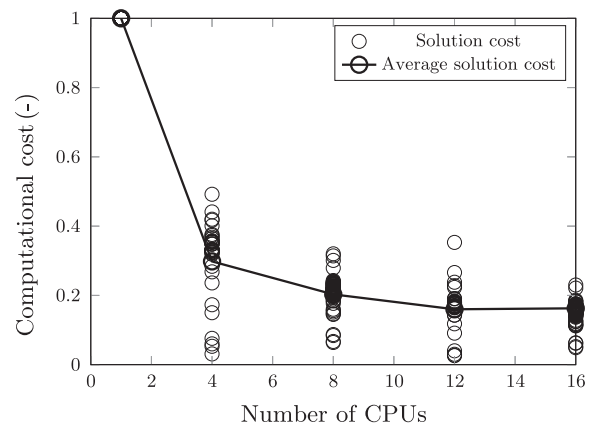


Fig. 8. Computation with difference number of CPUs using CSR + CGS.

6. In the sixth case (TM simulation), the model is computed considering that the dam is impermeable as it is mostly studied in concrete and composite dams. This case aims to quantify the separated effects of the water infiltration to the dam behaviors.

Six scenarios are compared and discussed in this section.

7.3. Displacement

The horizontal temporal displacements at the crest for different scenarios are presented in the Fig. 9. The numerical simulation results are compared with the measurements using a pendulum. As simulating the fully coupled THM problem in a standard case, the numerical simulation results have a good agreement with the measured results. It can be noticed that the control tunnel has an insignificant influence on the displacements. The numerical simulations considering the asphalt layer and the high viscosity liquid induce an increase in the displacement only under 0.1 mm at the steady state. However, when ignoring temperature effects in the numerical simulations, the displacement decreases significantly (over 2 mm at the final state), which can be interpreted as the temperature difference between the upstream side and the downstream side. The downstream side is exposed to the air, where temperature decreases from average 13 °C in summer to average 2 °C in winter (Fig. 4), while the upstream side was covered by water where temperature does not change significantly during the year (Fig. 3). Consequently, the temperature at the upstream side is generally higher than the temperature at the downstream side, and that leads to an increase of crest displacement. The simulation agrees with the discussion in [1]. The discussion shows that the change of ± 1 °C may change 0.21 mm deformation at the dam crest. When ignoring water infiltration in TM simulation, the shrinkage due to a decrease of suction (Eq. (10)), pore water pressure, and the change of material weight due to change of water content are not taken into account. Consequently, the displacement at the crest is smaller than the fully THM simulation.

7.4. Effective stress

The evolution of effective stress is presented in the Fig. 10, where pore-water pressure measured at the point G4 is plotted with the simulation results at the same coordinate. The effective stress decreases simultaneously with an increase of pore water pressure. The phenomenon is reproduced by Eq. (9). However, the simulation in the standard case does not totally fit with the measurement, the reasons could be measurement uncertainties

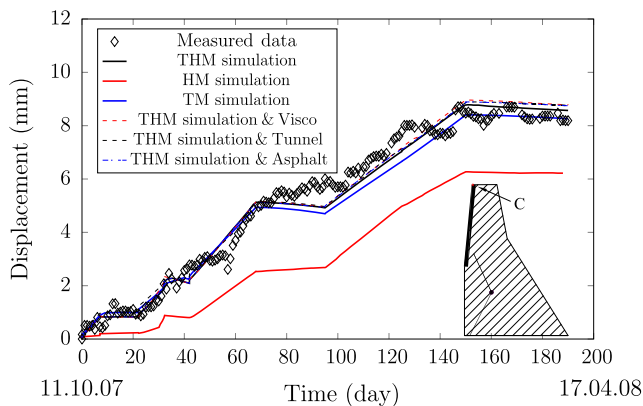


Fig. 9. Displacement at the crest (C) in Y direction.

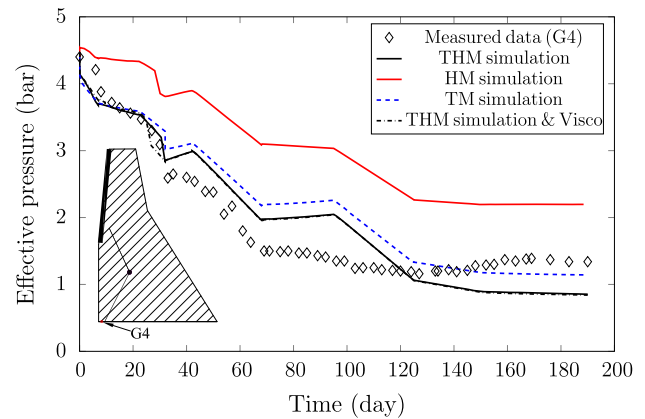


Fig. 10. The evolution of the effective pressure, G4(1.5, -1.5, -28.6) in meter.

and the initial temperature conditions are not fit with the real conditions. In fact, the initial temperature conditions in the dam body is non-uniform. We assume that the initial temperature is uniform over the whole volume. Therefore, the distribution of effective pressure in the dam body at the beginning as well as the final state is affected. It can be noticed that the effective pressure decreases more slowly when the temperature effects are not considered, while the simulations THM & Visco and THM & Asphalt show insignificant influences on the effective pressure. When ignoring the water infiltration into the dam structure, pore water pressure does not exist, therefore the result of effective pressure in TM simulation is greater than in THM simulation.

7.5. Temperature

The evolution of temperature is presented in the Fig. 11, where temperature measured at the points T1.1 and T1.2 are plotted with the simulation results at the same coordinate. It can be recognized that temperature at both points decreases with time. Temperature measured at point T1.1 decreases faster than the temperature measured at point T1.2, because the point T1.1 is located closer to the downstream side boundary. The simulation results confirm this statement. The simulation THM & Asphalt gives different results as compared with the THM standard simulation, where temperature is generally higher than the THM standard simulation. The

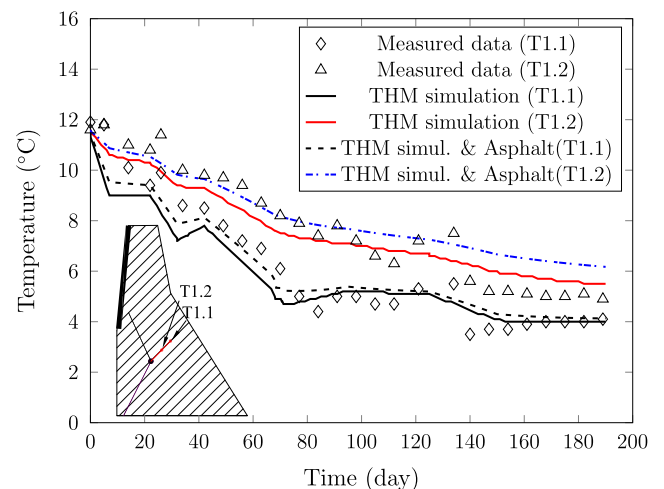


Fig. 11. The evolution of temperature, coordinate T1.1(-3.9, 8.3, -17.5) and T1.2(-3.9, 6.7, -18.9) in meter.

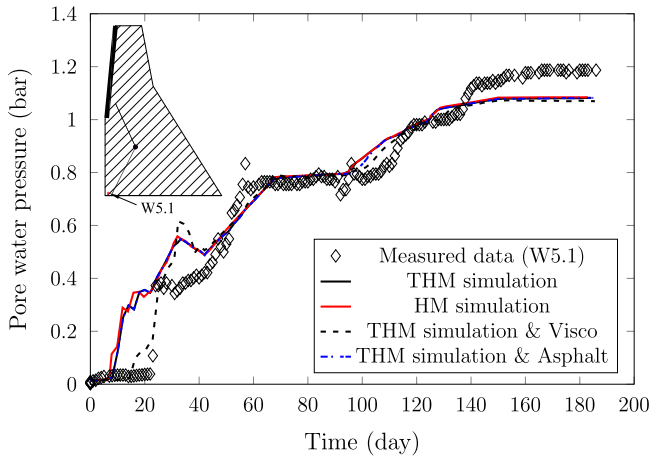


Fig. 12. The evolution of pore-water pressure, coordinate W5.1(−6.7, 0.9, −28.8) in meter.

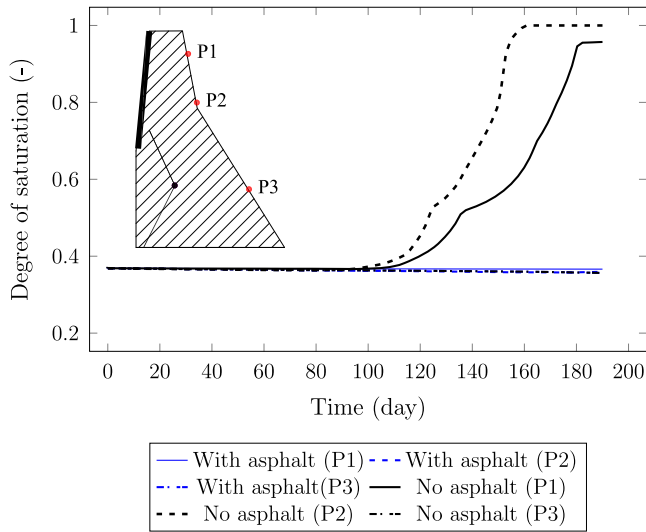


Fig. 13. The effect of asphalt layer on the infiltration process, coordinate P1(0.0, 4.4, −2.8), P2(0.0, 5.2, −7.5), and P3(0, 11.3, −18.5) in meter.

results can be interpreted by the thermal conductivity of the porous material. Thermal conductivity (λ_T) increases with the increase of water content. Without asphalt layers, the water infiltrates from the upstream side to the downstream side at the upper parts.

Water infiltration induces an increase of water content at the locations surrounding T1.1 and T1.2, and thus, increases the thermal conductivity. Consequently, the temperature at T1.1 and T1.2 decreases faster when asphalt layer is not considered in the simulation.

7.6. Pore-water pressure and state of wetness

The evolution of the pore water pressure is presented in the Fig. 12, where pore-water pressures measured at the point W5.1 are plotted with the simulation results at the same coordinate. It can be noticed that all scenarios of simulation gain the same final value of pore water pressure at steady state (when the water is filled to the top of the dam). However, changing the viscosity of the liquid affects significantly to the process of water infiltration. It can be interpreted according to generalized Darcy’s law (Eq. (11) and (12)), when the media is unsaturated, the relative permeability (k_{rl}) and liquid pressure vary according to the saturation. When the media is saturated, the parameter $k_{rl} = 1$, and consequently the gradient of liquid pressure converges to the steady state. The transition period from unsaturated condition to saturated condition of the point W5.1 and its surrounding regions is about 40 days. In this period, pore water pressure varies significantly. When the media is saturated, pore water pressure does not vary significantly and it follows closely the other scenarios as in Fig. 12.

The area of saturated region increases with water level and it is time dependent. The phenomenon of water infiltration is illustrated in the Fig. 13. When simulating without asphalt layer, the degree of saturation at points P1 and P2 increases to the maximum state while the degree of saturation at location P3 keeps constant at dry state. It is confirmed by the observations on the dam in Fig. 14(a), in which the wetting area is located on the upper parts of the dam. There are no wetting areas observed at the lower parts of the dam. The distribution of the degree of saturation at the final state is presented in the Fig. 14(b) and (c). Maximum degree of saturation is painted by brown red color (as in the left lower corner of the dam in Fig. 14(b)), minimum degree of saturation is painted by blue color (as in the right upper part of the dam in Fig. 14(b)). From Fig. 14(b) and (c), it can be noticed that the red brown zone is the saturated regions. It can be concluded from the figure that the drainage system works efficiently. It unloads the water pressure, and thus, helps to keep the lower part of the dam dry, while the asphalt layer is defected and allows water to infiltrate through the dam body from the upper part. High wetness in the dam structure may increase the ageing and weathering effects.

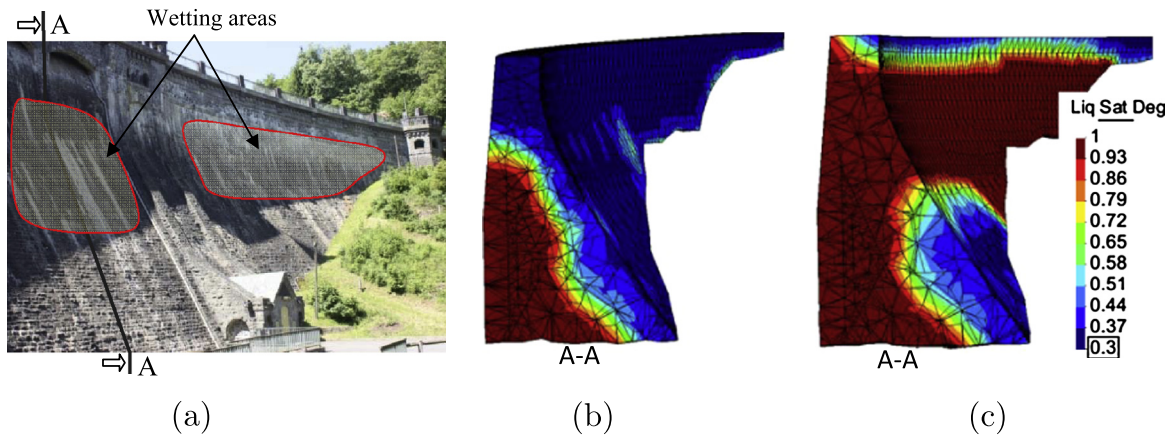


Fig. 14. Wetness after impounding process (190 days). (a) Wetting observed at downstream side. (b) Simulation with asphalt layer. (c) Simulation without asphalt layer.

8. Conclusions and outlook

In this paper, we introduce a fully coupled THM constitutive model of masonry materials applied to dams. We also present the numerical approaches and solutions for the system of equations. The solution method combining Compact Row Format as storage method with Pre-conditioned Conjugate Gradient Squared method proves an efficient method to reduce the computational cost. Furthermore, the parallel computation by means of openMP library improves significantly the time for solving the system of equations. Finally, the 3D numerical simulations are carried out for THM problems occurring at the Fürwigge dam.

The numerical simulation results show a good agreement with measured data in the evolution of displacements, effective pressure, temperature, and pore water pressure. The results prove the efficiency of the drainage system as a tool to unload the water pressure, and thereby, to keep the lower part of the dam dry. However, the deflection of asphalt layers allows the water to infiltrate in the upper part of the dam. For the outlook, the presented model is now assumed to be a valuable tool for the discussion of the effectiveness of new rehabilitation activities, e.g., improving the asphalt layer. This model can now be regarded as a reference model in related inverse problems, such as the identification of material properties and damages or cracks which may occur in the further lifetime of the structures, see [6]. The consideration of the variability of the material inside the structure and its effect to the structure's performance is subject to future research.

Acknowledgements

The research was supported by the Deutsche Forschungsgemeinschaft (DFG) under grant LA 2869/4-1 which is highly acknowledged by the authors. The measured data have been provided by the Ruhrverband Essen, Germany, which is also highly acknowledged by the authors.

Appendix A. Supplementary material

Supplementary data associated with this article can be found, in the online version, at <http://dx.doi.org/10.1016/j.compstruc.2016.10.007>.

References

- [1] Bettzieche V. Mathematisch-statistische Analyse von Messwerten der Talsperrenueberwachung. *Wasserwirtschaft* 2004;94(01–02):1–5.
- [2] Bettzieche V, Demisch G. Sanierung der Fürwiggetalsperre: Abschlussbericht zum Probestau. Tech. rep., Ruhrverband; 2008.
- [3] Risley JC, Constantz J, Essaid H, Rounds S. Effects of upstream dams versus groundwater pumping on stream temperature under varying climate conditions. *Water Resour Res* 2010;46(6):1–32. w06517.
- [4] Wang M, Chen Y-F, Hu R, Liu W, Zhou C-B. Coupled hydro-mechanical analysis of a dam foundation with thick fluvial deposits: a case study of the Danba Hydropower Project, Southwestern China. *Eur J Environ Civil Eng* 2016;20(1):19–44.
- [5] Azevedo ID, Vaz L, Vargas E. A numerical procedure for the analysis of the hydromechanical coupling in fractured rock masses. *Int J Numer Anal Methods Geomech* 1998;22:867–901.
- [6] Lahmer T. Crack identification in hydro-mechanical systems with applications to gravity water dams. *J Inverse Problems Sci Eng* 2010;18(8):1083–101.
- [7] Alonso EE, Olivella S, Pinyol NM. A review of Beliche dam. *Geotechnique* 2005;55(4):267–85.
- [8] Šýkora J, Vorel J, Krejčí T, Šejnoha M, Šejnoha J. Analysis of coupled heat and moisture transfer in masonry structures. *Mater Struct* 2009;42(8):1153–67.
- [9] Krus J, Krejčí T, Šýkora J, Šejnoha M. Computational homogenization of coupled heat and moisture transport on parallel computers civil comp proceedings 2015. In: Iványi P, Topping B, editors. Proc. of the ninth int. conference on engineering computational technology. Paper 25.
- [10] François B, Laloui L. ACMEG-TS: a constitutive model for unsaturated soils under non-isothermal conditions. *Int J Numer Anal Methods Geomech* 2008;32:1957–88.
- [11] Sánchez M, Gens A, Olivella S. THM analysis of a large-scale heating test incorporating material fabric changes. *Int J Numer Anal Methods Geomech* 2012;36(4):391–421.
- [12] Xiaoying Zhuang CL, Huang Runqiu, Rabczuk T. A coupled thermo-hydro-mechanical model of jointed hard rock for compressed air energy storage. *Math Problems Eng* 2014;. doi: <http://dx.doi.org/10.1155/2014/179169>179169.
- [13] Duff IS, Grimes RG, Lewis JG. Sparse matrix test problems. *ACM Trans Math Softw (TOMS)* 1989;15(1):1–14.
- [14] Sonneveld P. CGS, a Fast Lanczos-type Solver for nonsymmetric linear systems. *SIAM J Sci Stat Comput* 1989;10(1):36–52.
- [15] Šýkora J, Šejnoha M, Šejnoha J. Homogenization of coupled heat and moisture transport in masonry structures including interfaces. *Appl Math Comput* 2014;219(13):7275–85. {ESCO} 2010 conference in Pilsen, June 21–25, 2010.
- [16] Schanz T, Nguyen-Tuan L, Datcheva M. A column experiment to study the thermo-hydro-mechanical behaviour of expansive soils. *Rock Mech Rock Eng* 2013;46(6):1287–301.
- [17] Grifoll J, Gastó JM, Cohen Y. Non-isothermal soil water transport and evaporation. *Adv Water Resour* 2005;28(11):1254–66.
- [18] Pusch R. Permeability of highly compacted bentonite. Tech. rep., SKB Technical Report 80-16, Swedish Nuclear Fuel and Waste Management; 1980.
- [19] Wu W, Li X, Charlier R, Collin F. A thermo-hydro-mechanical constitutive model and its numerical modelling for unsaturated soils. *Comput Geotech* 2004;31:155–67.
- [20] Olivella S, Carrera J, Gens A, Alonso E. Non-isothermal multiphase flow of brine and gas through saline media. *Transport Porous Media* 1994;15:271–93.
- [21] Agus S, Arifin Y, Tripathy S, Schanz T. Swelling pressure–suction relationship of heavily compacted bentonite–sand mixtures. *Acta Geotech* 2013;8(2):155–65.
- [22] Brooks J. Concrete and masonry movements, no. Chapter 6. Butterworth-Heinemann; 2014.
- [23] Olivella S, Carrera J, Gens A, Alonso EE. Numerical formulation for a simulator (CODE_BRIGHT) for the coupled analysis of saline media. *Eng Comput* 1996;13:87–112.
- [24] van Genuchten MT. A closed-form equation for predicting the hydraulic conductivity of unsaturated soils. *Soil Sci Soc Am J* 1980;44:892–8.
- [25] van Genuchten M. A comparison of numerical solutions of the one-dimensional unsaturated-saturated flow and mass transport equations. *Adv Water Resour* 1982;5(1):47–55.
- [26] Lide DR. 85th CRC handbook of chemistry and physics. Boca Raton, FL: CRC Press, Inc.; 2005.
- [27] Sposito G. The thermodynamics of soil solution. University of California; 1981.
- [28] Zienkiewicz O, Taylor R. The finite element method: the basis. *Referex engineering*, 5th ed., vol. 1. Butterworth-Heinemann; 2000.
- [29] Milly P. A mass-conservative procedure for time-stepping in models of unsaturated flow. *Adv Water Resour* 1985;8(1):32–6.
- [30] Rabizadeh E, Bagherzadeh AS, Rabczuk T. Goal-oriented error estimation and adaptive mesh refinement in dynamic coupled thermoelasticity. *Comput Struct* 2016;173C:187–211.
- [31] Gens A, Garcia-Molina AJ, Olivella S, Alonso EE, Huertas F. Analysis of a full scale in situ test simulating repository conditions. *Int J Numer Anal Methods Geomech* 1998;22:515–48.